



Defect-anchored single-atom-layer Pt clusters on $\text{TiO}_{2-x}/\text{Ti}$ for efficient hydrogen evolution via photothermal reforming plastics

Di Jiang^{a,1}, Haifeng Yuan^{a,1}, Zhen Liu^{a,1}, Yuke Chen^a, Yangyang Li^c, Xiaoli Zhang^b, Guobin Xue^a, Hong Liu^{a,c}, Xiaoyan Liu^{a,*}, Lili Zhao^{a,*}, Weijia Zhou^{a,*}

^a Institute for Advanced Interdisciplinary Research (iAIR), School of Chemistry and Chemical Engineering, University of Jinan, Jinan 250022, PR China

^b School of Materials Science and Engineering, Zhengzhou University, Zhengzhou 450001, PR China

^c State Key Laboratory of Crystal Materials, Shandong University, 27 Shandan Road, Jinan, Shandong 250100, PR China

ARTICLE INFO

Keywords:

Laser synthesis
Defective titanium dioxide
Single-atom-layer Pt clusters
Photothermal catalysis
Reforming plastic

ABSTRACT

Hydrogen generation from plastics waste is a promising strategy to solve the plastic pollution crisis. Making full use of infrared energy of solar spectrum is an important subject for efficient solar photocatalysis. Herein, single-atom-layer Pt (SAL-Pt) clusters anchored on $\text{TiO}_{2-x}/\text{Ti}$ was used as photothermal catalyst to generate hydrogen from plastic in liquid conditions. The confinement effect of laser-regulated oxygen vacancies in $\text{TiO}_{2-x}/\text{Ti}$ plays an important role in anchoring SAL-Pt under mildly temperature and pressure condition. The obtained Pt/ $\text{TiO}_{2-x}/\text{Ti}$ possesses excellent photothermal catalytic hydrogen evolution performance from reforming plastic waste under infrared light ($273.12 \mu\text{mol cm}^{-2} \text{h}^{-1}$). The enhanced photothermal activity of Pt/ $\text{TiO}_{2-x}/\text{Ti}$ is due to enhanced infrared light absorption via plasmonic effect and hot electron aggregation on SAL-Pt from $\text{TiO}_{2-x}/\text{Ti}$. The practical applicability is further verified by photothermal catalytic reforming plastics to H_2 under ambient sunlight irradiation, which possesses high performance ($25.5 \mu\text{mol cm}^{-2} \text{h}^{-1}$) and stability (in consecutive week).

1. Introduction

In the past decades, the problem of environmental pollution had become more and more serious, due to the massive burning of fossil fuels [1]. Therefore, the development of new clean energy sources is crucial. Among many new energy sources, hydrogen energy with the major advantages of being clean, safe and pollution-free is widely produced by photocatalysis and electrocatalysis [2–5]. In addition, the plastic pollution crisis was also one of the biggest planet's environmental challenges [6,7]. These commercial plastic made from polymers played a huge role in our daily lives. But the natural degradation of these plastics often took hundreds of years, causing them to accumulate in the natural environment [8]. As a result, biodegradable plastics came into being [9]. Most degradable plastics began to be thin and break apart after exposure to normal environments for 3–6 months [10,11]. Therefore, recycling degradable plastics quickly is an urgent approach to be developed.

Using plastics waste as a feedstock for hydrogen generation was a

potential solution, which was considered as the most promising development strategy [12–14]. As well known, the infrared (IR) region accounts for more than 50 % of the full spectrum of sunlight [15,16]. However, most semiconductor photocatalysts had wide bandgap, such as TiO_2 (3.2 eV) [17,18], CdS (2.4 eV) [19–21] and ZnO (3.3 eV) [22], which could only catalyze reactions in the ultraviolet (UV) and visible (Vis) region. The energy in the IR region was mainly wasted and dissipated in the form of heat consumption. Therefore, it was an important problem to make full use of solar energy in the IR region. As a traditional semiconductor material, TiO_2 had the advantages of no photocorrosion, acid and alkali resistance, stable chemical properties, no toxicity to organisms and low price [18,23]. The introduction of oxygen vacancies could introduce a donor energy level below the conduction band of TiO_2 . Thus its band gap was width reduced and its light absorption range to visible and even infrared wavelengths was extended [24,25]. Several methods had been developed for preparing oxygen-deficient TiO_2 (TiO_{2-x}), such as hydrogen reduction treatment [26], active metal reduction [27], chemical reduction [28], electrochemical reduction

* Corresponding authors.

E-mail addresses: ifc_liuxy@ujn.edu.cn (X. Liu), ifc_zhaoll@ujn.edu.cn (L. Zhao), ifc_zhouwj@ujn.edu.cn (W. Zhou).

¹ These authors contributed equally to this work.

[29] and so on. While the construction of oxygen vacancy under mild conditions, and large-scale production were still necessary.

With the development of laser engineering, the construction of TiO_{2-x} by laser had attracted extensive attention [30–32]. Laser was a kind of high-energy light produced by the process of stimulated emission and light amplification [33–35]. With high energy density, laser could quickly create a high-temperature and high-pressure environment in a very small space, which was conducive to the synthesis and retention of oxygen vacancies [36,37]. Furthermore, the formation of oxygen vacancies on an ideal support was a significant approach for anchoring single atoms (SAs) or single-atom-layer (SAL) clusters [38,39]. This had been extensively researched for oxygen vacancies on metallic oxides anchoring noble metal atoms and clusters.

In this work, in-situ preparation of titanium oxide with rich oxygen vacancies on titanium foil ($\text{TiO}_{2-x}/\text{Ti}$) through focused laser ablation in air atmosphere has been proposed. The SAL-Pt clusters anchored $\text{TiO}_{2-x}/\text{Ti}$ ($\text{Pt}/\text{TiO}_{2-x}/\text{Ti}$) were synthesized by using oxygen vacancies as anchoring sites to atomically disperse metals through strong coordination interaction. Under the effect of maximum atom-utilization efficiency and enhanced infrared light absorption, the obtained $\text{Pt}/\text{TiO}_{2-x}/\text{Ti}$ had excellent photothermal hydrogen evolution performance. The hydrogen evolution of $\text{Pt}/\text{TiO}_{2-x}/\text{Ti}$ from reforming plastic under light irradiation with $\lambda > 760$ nm in liquid ($273.12 \mu\text{mol cm}^{-2} \text{h}^{-1}$) was approximately 17.2 times higher than that of the sample in the ultra-violet region ($15.87 \mu\text{mol cm}^{-2} \text{h}^{-1}$). The enhanced infrared light absorption via the plasmonic effect and the hot electron aggregation on SAL-Pt clusters from $\text{TiO}_{2-x}/\text{Ti}$ were confirmed. Therefore, the construction of oxides with oxygen vacancies through laser processing and fully exposed single-atom-layer clusters may provide a new method for creating efficient photothermal catalysts, which expand the utilization of plastic wastes and stimulate new strategies for recycling plastic wastes.

2. Experimental section

2.1. Synthesis of titanium dioxide with oxygen vacancies ($\text{TiO}_{2-x}/\text{Ti}$) by laser ablation process under air atmosphere

Firstly, in order to remove the oxide and grease on pristine Ti foil (99.9 % purity), mechanical polishing and ultrasonic cleaning were carried out with acetone, diluted hydrochloric acid and deionized H_2O for 30 min, respectively. Next, the fiber laser system (LSF20D/20, HGTECH) with the pulse duration of 100 ns and the laser wavelength of 1064 nm was used to generate TiO_{2-x} with oxygen vacancies on the surface of Ti foil ($\text{TiO}_{2-x}/\text{Ti}$) with the diameter of 1.5 cm under air atmosphere. Single pulse energy of 0.5 mJ, average power of 8 W, linear scanning mode with the repetition rate of 30 kHz, scanning speed of 200 mm s^{-1} and scanning spacing of 0.1 mm were used to draw the patterns with EzCad2 software. The TiO_2 without oxygen vacancies on Ti foil (TiO_2/Ti) was synthesized in the same way, but the scanning speed was 50 mm s^{-1} with the average power of 6 W, and under an oxygen atmosphere.

2.2. Synthesis of single-atomic-layer Pt clusters loaded on $\text{TiO}_{2-x}/\text{Ti}$ ($\text{Pt}/\text{TiO}_{2-x}/\text{Ti}$)

First, a chloroplatinic acid hexahydrate ($\text{H}_2\text{Cl}_6\text{Pt} \cdot 6\text{H}_2\text{O}$, Aldrich) solution with the concentration of 5 mM was prepared by dissolving it in stirred deionized H_2O . Then, the prepared circular $\text{TiO}_{2-x}/\text{Ti}$ with the diameter of 1.5 cm was immediately immersed in 1 mL 5 mM $\text{H}_2\text{Cl}_6\text{Pt} \cdot 6\text{H}_2\text{O}$ solution without any further treatments. Next, it was rinsed with deionized water and naturally dried.

2.3. Photothermal hydrogen evolution by reforming plastic

The photothermal H_2 generation in collaboration with plastic

reforming were performed in a closed quartz-bottomed flask. The volume of the quartz reactor in the photothermal catalysis experiment was 50 mL, and 20 mL volume of NaOH treatment solution were added to the quartz reactor. The photothermal experiment was performed by using a 250 W infrared lamp (PHILIPS BR125 250 W, $0.76\text{--}5 \mu\text{m}$) as light source that was set away from the reactor with 10 cm. The photocatalytic experiment was performed by using a 300 watt xenon arc lamp that equipped with a 400–800 nm UV-IR cut-off glass light filter (i.e., $400 \text{ nm} < \lambda < 800 \text{ nm}$) or using 365 nm single wavelength UV lamp (i.e., $\lambda = 365 \text{ nm}$). The light intensity of different regions of UV, Vis and IR remained the same of 460 mW/cm^2 which was measured by an optical power meter.

The 20 mg mL^{-1} degradable plastic were dissolved in 10 M NaOH with the temperature of 40°C and stirred for 24 h in air. Then, the as-prepared catalysts with the diameter of 1.5 cm and degradable plastic solution were added into the quartz container. Before irradiation, air was removed by blowing nitrogen bubbles for 30 min. During the catalysis process, on-line gas chromatograph (GC-7900, Cealight) was used to detect the amounts of hydrogen evolution. During the catalysis test, the closed batch reactor for catalytic reaction was used and the product gas was withdrawn from the reactor at 20 min, 40 min, 60 min and 80 min, respectively. The product rate was obtained by a linear fit of yields through time. The production of CH_4 , CO, and CO_2 were measured by gas chromatography with a flame ionization detector (GC, Agilent GC 7890B). For further evaluating the photothermal hydrogen evolution performance of $\text{Pt}/\text{TiO}_{2-x}$, the catalyst were scraped off from the titanium sheet to get the quality. In order to ensure the rationality of the data, the average value of the three data was obtained as the quality of the $\text{Pt}/\text{TiO}_{2-x}$ ($1.24 \pm 0.16 \text{ mg}$).

For the photothermal catalytic H_2 by reforming plastic under ambient sunlight irradiation, the linear fresnel len with the area of $25 \times 25 \text{ cm}^2$ was used for the concentrator of sunlight. And the experiment was carried in consecutive week (13:00–14:00 pm) on May, 2022, in Jinan City, China.

3. Results and discussion

3.1. Structural characterization of SAL-Pt clusters anchored on $\text{TiO}_{2-x}/\text{Ti}$

The titanium oxides with oxygen vacancies on Ti foil ($\text{TiO}_{2-x}/\text{Ti}$) were generated by a focused high-energy nanosecond pulsed laser, as shown in Fig. 1a and Fig. S1. The synthesis process and the corresponding physical pictures were illustrated in Fig. S2. As shown in Fig. 1a, the high-energy focused pulsed laser could heat the titanium target and excite the surrounding air or oxygen gas to produce gaseous plasma at the titanium target interface [36]. Then the plasma ions interacted with Ti in the plasma zone to form titanium oxides. Due to insufficient oxygen at the interface between Ti foil and air, the $\text{TiO}_{2-x}/\text{Ti}$ with oxygen vacancies was synthesized. The laser-synthesized TiO_2/Ti without oxygen vacancies under pure oxygen atmosphere and $\text{TiO}_{2-x}/\text{Ti}$ with oxygen vacancies under air atmosphere were white (inset of Fig. S3a) and blue (inset of Fig. S3b), respectively, due to the different amount of oxygen vacancies. Moreover, the presence of oxygen vacancies in $\text{TiO}_{2-x}/\text{Ti}$ was confirmed by electron paramagnetic resonance (EPR) and Raman spectroscopy, as shown in Fig. S3. X-ray diffraction (XRD) patterns in Fig. S3g revealed that both TiO_2/Ti and $\text{TiO}_{2-x}/\text{Ti}$ were well coincident with anatase TiO_2 (JCPDS No. 73-1764) and rutile TiO_2 (JCPDS No. 75-1751), and without other impurities.

Furthermore, single-atom-layer Pt (SAL-Pt) clusters anchored $\text{TiO}_{2-x}/\text{Ti}$ ($\text{Pt}/\text{TiO}_{2-x}/\text{Ti}$) were synthesized by simply immersion it in a dilute hexachloroplatinic acid solution (Fig. 1a), which due to strong coordination interaction and confinement effect of oxygen vacancies as anchoring sites [40]. As shown in Fig. 1a, the generated oxygen vacancies could serve as the “traps” to capture and stabilize the Pt atoms via confinement-anchoring effect [41], which could be carried out under

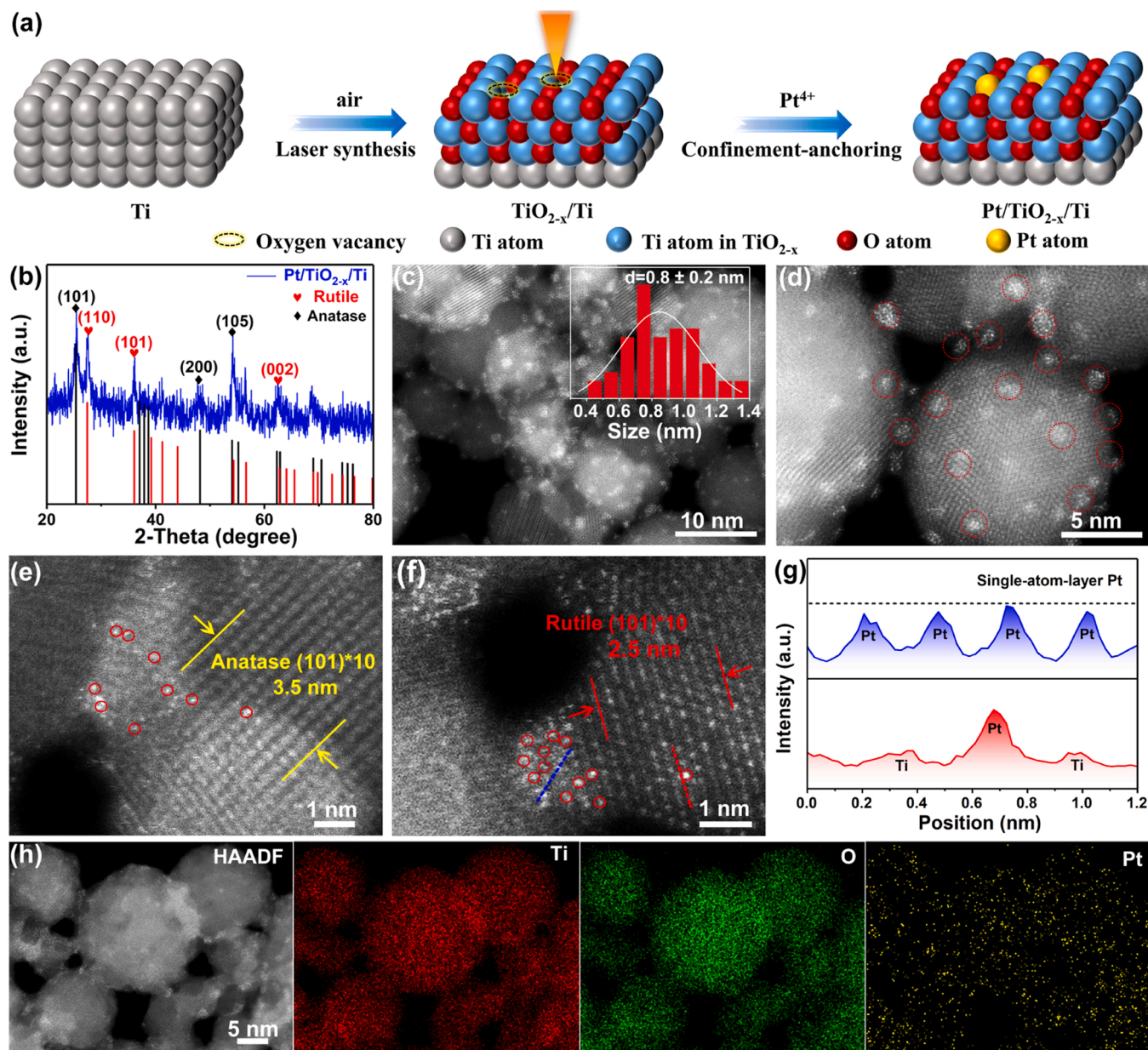


Fig. 1. (a) Synthesis process of Pt/TiO_{2-x}/Ti by laser-induced confinement-anchoring effect. (b) XRD pattern and (c-f) HAADF-STEM images of Pt/TiO_{2-x}/Ti. Inset of 1c was the corresponding particle size distribution of SAL-Pt clusters. (g) The corresponding extracted line profiles along with the blue (Pt clusters) and red (Pt single atom) line directions. (h) HAADF-STEM and according mapping images of Ti, O, Pt elements for Pt/TiO_{2-x}.

mild room temperature conditions without high-heat treatment. The SEM images in Fig. S4 showed the loading of Pt did not destroy the original nanostructure of TiO_{2-x}/Ti, and no apparent Pt nanoparticles were observed. The XRD pattern of Pt/TiO_{2-x}/Ti in Fig. 1b also displayed unchanged phases of rutile and anatase, and no corresponding Pt species were detected because of its ultralow loading amount. However, the color became from blue of TiO_{2-x}/Ti to wathet blue of Pt/TiO_{2-x}/Ti, indicating the successful loading of Pt onto TiO_{2-x}/Ti (Fig. S4). The Pt loading on Pt/TiO_{2-x}/Ti was determined to be 1.58 wt% by inductively coupled plasma (ICP) spectrometry (Table S1).

High-angle aberration-corrected annular dark-field scanning TEM (AC HAADF-STEM) was performed to directly observe the diffusion of Pt species in Pt/TiO_{2-x}/Ti. The HAADF-STEM images showed that Pt/TiO_{2-x} were composed of TiO_{2-x} nanoparticles and Pt clusters as the bright spots (Fig. 1c). The uniformly dispersed Pt clusters were well distinguished as closely connected “islands” with a small size of $\approx 0.8 \pm 0.2$ nm (inset of Fig. 1c). As shown in Fig. 1d and Fig. S5, single-atom-

layer Pt (SAL-Pt) clusters (bright dots circled with red line) were highly dispersed on TiO_{2-x} support. The magnified HAADF-STEM image clearly disclosed that uniformly dispersed Pt clusters were anchored on the (101) crystal plane of anatase TiO₂ (Fig. 1e) and (101) crystal plane of rutile TiO₂ (Fig. 1f). Pt atoms could be directly observed due to their higher Z-contrast than the neighboring Ti atoms, the extracted red line suggested the Pt single atoms decorated in Ti without significant alteration its lattice structure. Furthermore, the extracted blue line revealed that the Pt clusters were monolayer atomic structure (Fig. 1g), which gave them fully exposed characteristics [42,43]. The energy-dispersive X-ray spectroscopy (EDS) elemental mapping in Fig. 1h showed that Ti, O and Pt were homogeneously distributed on Pt/TiO_{2-x}, which provided additional evidence that SAL-Pt clusters were highly dispersed.

The surface chemical composition and valence state of Pt/TiO_{2-x}/Ti were analyzed by XPS spectra in Fig. 2a, b and S6. As shown in Fig. 2a, the Pt element was detected for Pt/TiO_{2-x}/Ti, but no spectra of Pt were identified in TiO_{2-x}/Ti. The binding peaks of Pt 4f_{5/2} (77.4 eV, 75.8 eV),

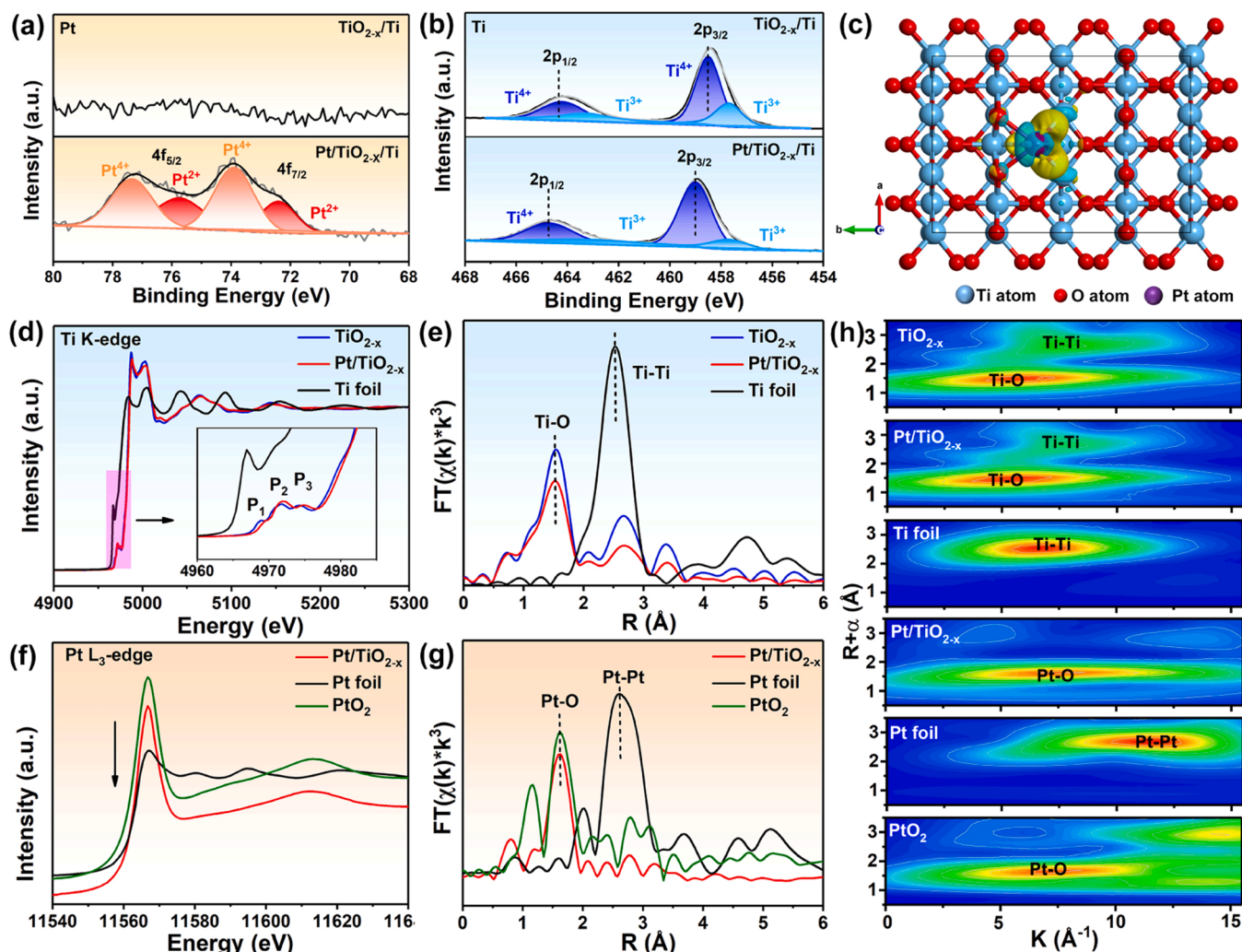


Fig. 2. High-resolution XPS spectra of (a) Pt 4f and (b) Ti 2p of $\text{TiO}_{2-x}/\text{Ti}$ and $\text{Pt}/\text{TiO}_{2-x}/\text{Ti}$. (c) Difference charge density of $\text{Pt}/\text{TiO}_{2-x}$ (the yellow region represents the electron accumulation, while the green region represents the electron depletion). (d) Ti K-edge XANES spectra and (e) FT-EXAFS spectra of $\text{TiO}_{2-x}/\text{Ti}$, $\text{Pt}/\text{TiO}_{2-x}/\text{Ti}$, Ti foil. (f) Pt $\text{L}_{3\text{-edge}}$ XANES spectra and (g) FT-EXAFS spectra of $\text{Pt}/\text{TiO}_{2-x}/\text{Ti}$, Pt foil and PtO_2 . (h) Ti K-edge WT-EXAFS of $\text{TiO}_{2-x}/\text{Ti}$, $\text{Pt}/\text{TiO}_{2-x}/\text{Ti}$, Ti foil and Pt $\text{L}_{3\text{-edge}}$ WT-EXAFS of $\text{Pt}/\text{TiO}_{2-x}/\text{Ti}$, Pt foil and PtO_2 .

Pt $4f_{7/2}$ (73.9 eV, 72.4 eV) detected in $\text{Pt}/\text{TiO}_{2-x}/\text{Ti}$ were corresponding well with Pt^{4+} and Pt^{2+} species, respectively. However, the binding peaks of Pt^0 were not detected, indicating that no Pt nanoparticles were formed. In Fig. 2b, compared to $\text{TiO}_{2-x}/\text{Ti}$, the peak area of Ti^{3+} in $\text{Pt}/\text{TiO}_{2-x}/\text{Ti}$ was obviously lower, implying the anchored effect of the oxygen vacancies. In addition, compared to $\text{TiO}_{2-x}/\text{Ti}$ (458.5 eV), the peak of Ti^{4+} shifted to higher energy in $\text{Pt}/\text{TiO}_{2-x}/\text{Ti}$ (459.0 eV), implying that the electrons were transferred from TiO_{2-x} to Pt. The difference charge density of $\text{Pt}/\text{TiO}_{2-x}/\text{Ti}$ in Fig. 2c also verified that the electrons accumulated onto the Pt atom due to its electronegativity difference.

The X-ray absorption near-edge spectroscopy (XANES) spectra of Ti K-edge and Pt $\text{L}_{3\text{-edge}}$ were performed to study the local structural variation of Ti and Pt species in $\text{TiO}_{2-x}/\text{Ti}$ and $\text{Pt}/\text{TiO}_{2-x}/\text{Ti}$. As shown in Fig. 2d, the three pre-edge peaks (P_1 , P_2 and P_3) corresponded to the quadruple-allowed Ti 1 s-3d electronic transitions [44]. Compared with $\text{TiO}_{2-x}/\text{Ti}$, the absorption of Ti K-edge in the pre-edge of $\text{Pt}/\text{TiO}_{2-x}/\text{Ti}$ obviously shifted to the higher energy direction, implying the valence of Ti species was higher, and the strong electron transfer from $\text{TiO}_{2-x}/\text{Ti}$ to SAL-Pt clusters [45]. Fig. 2e displayed the FT-EXAFS spectrum of Ti K-edge in Ti foil, $\text{TiO}_{2-x}/\text{Ti}$ and $\text{Pt}/\text{TiO}_{2-x}/\text{Ti}$. The peaks at 1.5 Å and 2.5 Å were associated with Ti-O coordination and Ti-Ti coordination, respectively. As shown in the Wavelet Transform (WT) profiles of the Ti

foil, $\text{TiO}_{2-x}/\text{Ti}$ and $\text{Pt}/\text{TiO}_{2-x}/\text{Ti}$ (Fig. 2h), the intensity at 7.8 Å^{-1} and 6.8 Å^{-1} belonged to the Ti-O contribution and Ti-Ti contribution, respectively.

From normalized XANES curves of Pt $\text{L}_{3\text{-edge}}$, the white line intensity of the $\text{Pt}/\text{TiO}_{2-x}$ was lower than that of PtO_2 and higher than that of Pt foil (Fig. 2f). The results revealed that Pt species in the $\text{Pt}/\text{TiO}_{2-x}$ carried partially positive charge, which further indicated that charge transfer occurred between SAL-Pt clusters and O atoms via metal-support interaction (MSI) effect [46–49]. As shown in Fig. 2g, the FT-EXAFS plots of the $\text{Pt}/\text{TiO}_{2-x}$ only displayed an obvious peak at 1.6 Å, which was the result of Pt-O coordination. In addition, no peaks (2.6 Å) related to Pt-Pt coordination were detected, suggesting that only SAL-Pt clusters existed. It could be seen from the WT contour plots of the Pt foil and PtO_2 (Fig. 2h) that the maximum intensity at 7.5 Å^{-1} and 14.3 Å^{-1} belonged to the contribution of Pt-O and Pt-Pt. Furthermore, the WT plots of the $\text{Pt}/\text{TiO}_{2-x}$ showed the maximum intensity at 7.5 Å^{-1} , which was assigned as Pt-O coordination. The above results further solidly indicated that SAL-Pt clusters were introduced onto $\text{Pt}/\text{TiO}_{2-x}/\text{Ti}$, which were present in the form of Pt-O bonds.

3.2. Photothermal performance

For both photocatalysts and photothermal catalysts, the light

absorption was a necessary prerequisite. The three-dimensional nanostructures of $\text{TiO}_{2-x}/\text{Ti}$ and $\text{Pt}/\text{TiO}_{2-x}/\text{Ti}$ could enhance the absorbability of light, reduce the reflection and elongate the optical path for multiple scattering [50]. The UV-Vis-NIR absorption spectra of TiO_2/Ti , $\text{TiO}_{2-x}/\text{Ti}$ and $\text{Pt}/\text{TiO}_{2-x}/\text{Ti}$ were shown in Fig. 3a. The UV-Vis-NIR absorption spectra of TiO_2/Ti without oxygen vacancies exhibited only absorption in the UV irradiation range from 200 nm to 420 nm. While the significant absorption throughout the UV-Vis-NIR wavelength range of 200–1500 nm were observed for the $\text{TiO}_{2-x}/\text{Ti}$ and $\text{Pt}/\text{TiO}_{2-x}/\text{Ti}$, which were mainly due to the existence of oxygen vacancies and the light trapping effect of nanostructures [30]. It was worth noting that $\text{TiO}_{2-x}/\text{Ti}$ exhibited even better absorption than that of $\text{Pt}/\text{TiO}_{2-x}/\text{Ti}$, which might be due to the loading of SAL Pt clusters on the surface of $\text{TiO}_{2-x}/\text{Ti}$ would consume partial of oxygen vacancies and then hinder the light absorption in IR region and a small range of Vis region. Moreover, the plots of $(F(R)E)^{1/2}$ were taken to calculate the band gap of TiO_2/Ti , $\text{TiO}_{2-x}/\text{Ti}$ and $\text{Pt}/\text{TiO}_{2-x}/\text{Ti}$ (Fig. S7). For TiO_2/Ti , $\text{TiO}_{2-x}/\text{Ti}$ and $\text{Pt}/\text{TiO}_{2-x}/\text{Ti}$, the almost unchanged band gap widths of ≈ 3.1 eV were calculated due to the intrinsic absorption of TiO_2 . The surface oxygen vacancies could introduce intraband gap defect states, thus enhanced the absorption of Vis-NIR irradiation [51,52].

Photothermal transformation was an important property of the photothermal catalysis. In Fig. 3b and e, the according surface temperature profiles of TiO_2/Ti (I), $\text{TiO}_{2-x}/\text{Ti}$ (II) and $\text{Pt}/\text{TiO}_{2-x}/\text{Ti}$ (III) under

the UV irradiation showed no significant difference of their temperatures, which were basically the same around 40°C within 180 s. Under the light wavelength of $400\text{ nm} < \lambda < 800\text{ nm}$ (Fig. 3c), the according temperature distribution curves of TiO_2/Ti , $\text{TiO}_{2-x}/\text{Ti}$ and $\text{Pt}/\text{TiO}_{2-x}/\text{Ti}$ in Fig. 3f also showed the similar temperatures of 66.8°C , 71.2°C and 79.2°C within 180 s, respectively. Under the irradiation of an infrared lamp ($\lambda > 760\text{ nm}$), as shown in Fig. 3d and g, the $\text{Pt}/\text{TiO}_{2-x}/\text{Ti}$ reached the highest temperature of 311.7°C within 50 s, which was higher than those of the TiO_2/Ti (181.5°C) and $\text{TiO}_{2-x}/\text{Ti}$ (271.8°C) under the same condition. The results confirmed that the oxygen vacancies and SAL Pt clusters loading evidently enhanced photothermal conversion under IR irradiation.

As was well-known that photocurrent test was an efficient technique for evaluating the excitation of electron-hole pairs and characterizing the separation of carriers [57,58]. As shown in Fig. 3h, the $\text{Pt}/\text{TiO}_{2-x}/\text{Ti}$ performed the highest photocurrent density of 0.56 mA cm^{-2} under the UV irradiation than those of TiO_2/Ti and $\text{TiO}_{2-x}/\text{Ti}$. The results implied that the $\text{Pt}/\text{TiO}_{2-x}/\text{Ti}$ had the longest photo-induced electron-hole pairs lifetime. The photocurrents of TiO_2/Ti (0.051 mA cm^{-2}), $\text{TiO}_{2-x}/\text{Ti}$ (0.069 mA cm^{-2}) and $\text{Pt}/\text{TiO}_{2-x}/\text{Ti}$ (0.081 mA cm^{-2}) under the visible light irradiation ($400\text{ nm} < \lambda < 800\text{ nm}$) were very small, because that the visible light was hard to excite TiO_2/Ti to produce photogenerated electron-hole pairs (Fig. 3i). As shown in Fig. 3j, the large photocurrent responses were detected under light irradiation with $\lambda > 760\text{ nm}$, which

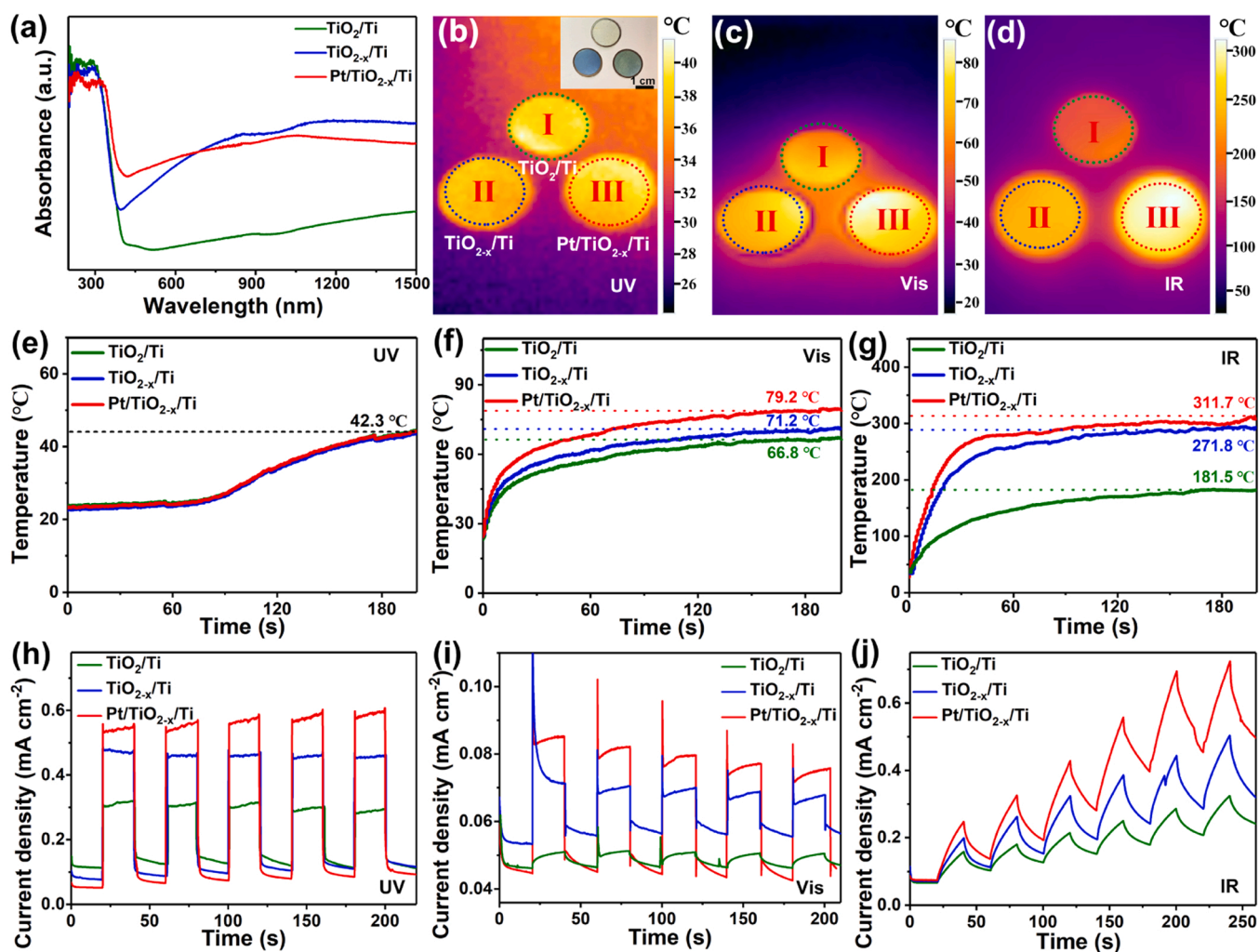


Fig. 3. (a) UV-Vis-NIR absorption spectra of TiO_2/Ti , $\text{TiO}_{2-x}/\text{Ti}$ and $\text{Pt}/\text{TiO}_{2-x}/\text{Ti}$. Infrared thermal images, according surface temperature profiles and transient photocurrent responses of TiO_2/Ti (I), $\text{TiO}_{2-x}/\text{Ti}$ (II) and $\text{Pt}/\text{TiO}_{2-x}/\text{Ti}$ (III) with the diameter of 1.5 cm under light irradiation with (b, e, h) $\lambda = 365\text{ nm}$ (UV), (c, f, i) $400\text{ nm} < \lambda < 800\text{ nm}$ (Vis) and (d, g, j) $\lambda > 760\text{ nm}$ (IR), respectively.

possessed the value size sort of Pt/TiO_{2-x}/Ti (0.72 mA cm⁻²) > TiO_{2-x}/Ti (0.5 mA cm⁻²) > TiO₂/Ti (0.32 mA cm⁻²) at 250 s, indicating that both oxygen vacancies and Pt loading simultaneously contributed to the photocurrent responses. It could be owing to the synergistic effect between the photothermic effect of TiO_{2-x} and the plasma resonance of Pt under infrared irradiation [46,53]. In addition, the photocurrent showed an overall increasing trend was noted, which might be due to the increased electrolyte temperature.

In addition, the Kelvin probe force microscopy (KPFM) was used to confirm the surface potential of Pt/TiO_{2-x}/Ti under dark and IR illumination (Fig. S8). Under IR illumination, the surface potential of Pt/TiO_{2-x}/Ti increased about 60 mV, as shown in Fig. S8. These results suggested that the loading of SAL Pt clusters was conducive to separate hot carrier pairs produced from the TiO_{2-x} with IR light excitation [54–56].

3.3. Hydrogen evolution performance by reforming plastics in liquid

Since the plastic wastes had caused serious damage, it was imperative to developing new strategies for recycling or degrading these plastic wastes. Hence, the hydrogen evolution by reforming plastic in liquid under light irradiation with $\lambda = 365$ nm (UV), $400 \text{ nm} < \lambda < 800$ nm

(Vis) and $\lambda > 760$ nm (IR) were performed to evaluate catalytic hydrogen production performance in Fig. 4a. The TiO₂/Ti, TiO_{2-x}/Ti and Pt/TiO_{2-x}/Ti possessed the poor catalytic performance under UV (16.14, 11.02, 20.6 $\mu\text{mol cm}^{-2} \text{ h}^{-1}$) and visible light radiation (0, 4.09, 11.89 $\mu\text{mol cm}^{-2} \text{ h}^{-1}$), which were much lower than that under infrared light radiation. Under the infrared light irradiation, TiO_{2-x}/Ti exhibited hydrogen production rate of 55.88 $\mu\text{mol cm}^{-2} \text{ h}^{-1}$, and was higher than that of TiO₂/Ti (25.93 $\mu\text{mol cm}^{-2} \text{ h}^{-1}$). The introduction of SAL-Pt clusters as the catalytic site resulted in Pt/TiO_{2-x}/Ti exhibited the highest catalytic activity with hydrogen production rate of 273.12 $\mu\text{mol cm}^{-2} \text{ h}^{-1}$, which was almost 11 times and 5 times than those of TiO₂/Ti and TiO_{2-x}/Ti, respectively. In order to further determine the interaction between IR light-induced photochemical effect and thermochemical effect, the corresponding control variable experiment were tested. As shown in Fig. S9, the solution temperature with Pt/TiO_{2-x}/Ti catalyst was 100 °C under light irradiation with $\lambda > 760$ nm. When the system was heated via oil bath to 100 °C without light irradiation, the hydrogen evolution with Pt/TiO_{2-x}/Ti catalyst was only 19.98 $\mu\text{mol cm}^{-2} \text{ h}^{-1}$ (Fig. S10). In addition, when Pt/TiO_{2-x}/Ti was under light irradiation with $\lambda > 760$ nm and the temperature was kept at 20 °C with a cooling circulating water system, the hydrogen production rate was only 1.5 $\mu\text{mol cm}^{-2} \text{ h}^{-1}$. These results confirmed that both heat and light could

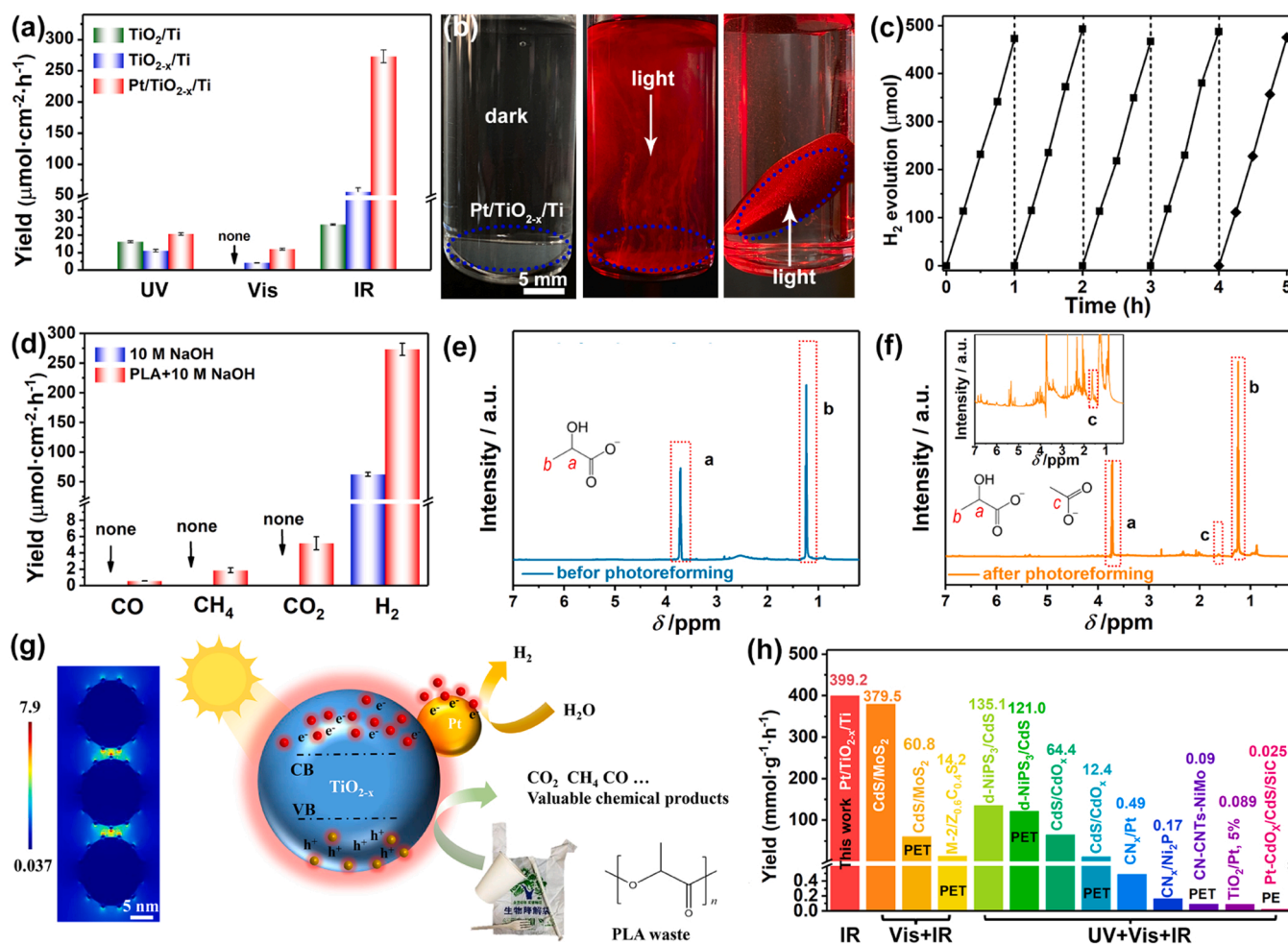


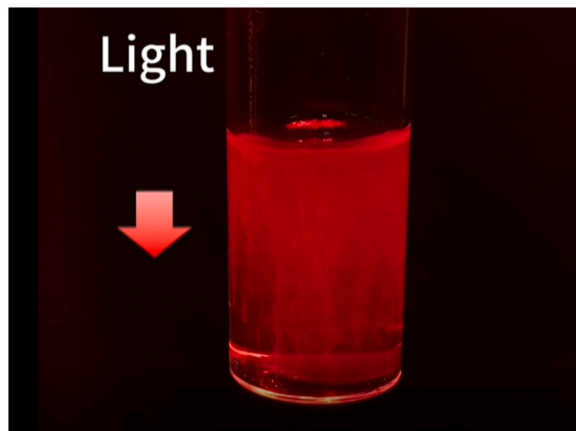
Fig. 4. (a) Hydrogen evolution rates of TiO₂/Ti, TiO_{2-x}/Ti and Pt/TiO_{2-x}/Ti by reforming plastics under light irradiation with $\lambda = 365$ nm (UV), $400 \text{ nm} < \lambda < 800$ nm (Vis) and $\lambda > 760$ nm (IR). (b) The optical diagrams of Pt/TiO_{2-x}/Ti for producing hydrogen under light irradiation with $\lambda > 760$ nm. (c) Recycling test of Pt/TiO_{2-x}/Ti by reforming plastic under light irradiation with $\lambda > 760$ nm. (d) The gas evolution rates of CO, CH₄, CO₂ and H₂ by reforming plastics and using Pt/TiO_{2-x}/Ti as catalysts under light irradiation with $\lambda > 760$ nm. ¹H NMR spectra of PLA before (e) and after (f) PR for 24 h under infrared irradiation with Pt/TiO_{2-x}/Ti in 10 M NaOD in D₂O (3 mL). (g) Schematic diagram of reforming plastic for hydrogen evolution. Inset was Finite-difference time-domain (FDTD) result of near-field electromagnetic field distributions at 785 nm in Pt/TiO_{2-x}. (h) Comparison of the H₂ evolution of Pt/TiO_{2-x}/Ti in this work with previously reported catalysts.

participate in the hydrogen evolution reaction by reforming plastics. Furthermore, the hydrogen production of Pt/TiO_{2-x}/Ti under light irradiation with $\lambda > 760$ nm without the NaOH pretreatment solution was performed and no hydrogen was produced. The plastic dispersed in the form of small solid particles rather than monomers increased the difficulty of adsorption on the catalyst surface and the degree of oxidation.

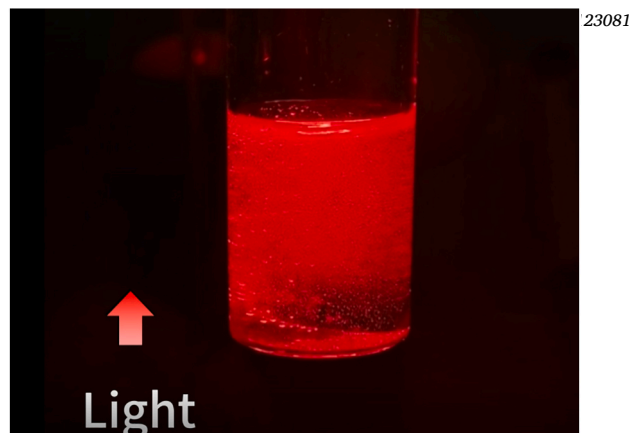
The optical pictures of hydrogen production during the test under light irradiation with $\lambda > 760$ nm were shown in Fig. 4b. The curves of H₂ production rate depending on the time taken were shown in Fig. S11, the H₂ product for Pt/TiO_{2-x}/Ti were continuously generated over time. A large number of bubbles could be seen emerging from the surface of Pt/TiO_{2-x}/Ti sheet as time went on (Video S1). Noted that the Pt/TiO_{2-x}/Ti sheet could be jacked up by bubbles, when the catalyst was faced down and the light was irradiated from the bottom (Video S2). In Fig. 4c, the 5 h catalytic recycling tests of Pt/TiO_{2-x}/Ti under light irradiation with $\lambda > 760$ nm by reforming plastic showed no significant performance degradation during 5 runs of tests. The XRD (Fig. S12), XPS (Fig. S13), SEM (Fig. S14) and optical image (Fig. S15) after the catalytic reaction showed no significant changes in surface elements and crystal structure, confirming the catalytic stability and structure stability of Pt/TiO_{2-x}/Ti.

In order to confirm the hydrogen was produced from reforming plastics, the hydrogen evolution rates of Pt/TiO_{2-x}/Ti with and without plastic in 10 M NaOH under infrared irradiation were performed in Fig. 4d. There was only H₂ (62.28 $\mu\text{mol cm}^{-2} \text{h}^{-1}$) be detected in 10 M NaOH without plastic, which was much lower than that (273.12 $\mu\text{mol cm}^{-2} \text{h}^{-1}$) with plastic in 10 M NaOH, implying the promoting effect through reforming plastics. As for gas products, except for hydrogen, including CO₂ (5.17 $\mu\text{mol cm}^{-2} \text{h}^{-1}$), CO (0.55 $\mu\text{mol cm}^{-2} \text{h}^{-1}$) and CH₄ (1.86 $\mu\text{mol cm}^{-2} \text{h}^{-1}$) were also detected, indicating that partial plastics were oxidized and reformed into various gas products. It was crucial to generate high-value organic products through controlling the oxidation half-reaction. Thus, the ¹H NMR spectroscopy was performed to identify reaction mixtures and organic oxidation products. As for liquid phase products, waste plastics would firstly hydrolyze to lactate during pre-treatment (peaks a, b), which was then oxidized to acetate (peak c) and other unidentified products (Fig. 4e, f).

On the basis of above results, the mechanism of reforming plastic under the irradiation with $\lambda > 760$ nm for Pt/TiO_{2-x}/Ti was illustrated in Fig. 4g. Firstly, TiO_{2-x}/Ti with oxygen vacancies and nanostructures could effectively absorbed infrared light to excite the generation of hot electrons and convert photo-to-heat under infrared irradiation. Secondly, hot electrons could be transferred to SAL-Pt clusters and the thermal catalytic reaction occurred. Water was reduced for hydrogen production on SAL-Pt clusters, and pre-treated plastics were decomposed into small molecules of O₂, CO, CH₄, acetate and other



Video S1. Video S1 illustrated the rapid production of hydrogen emerging from the surface of Pt/TiO_{2-x}/Ti sheet via photothermal reforming plastic with infrared irradiated from the top..



Video S2. Video S2 illustrated that Pt/TiO_{2-x}/Ti sheet could be jacked up by bubbles via photothermal reforming plastic with the catalyst was facing down and infrared irradiated from the bottom..

unidentified products by photothermal catalysis. The electromagnetic near-field distributions at the catalytic interface was also simulated by using Finite-difference time-domain (FDTD) simulation and assisting with mechanism explanations in plasmonic hot electrons for efficient hydrogen evolution. Inset of Fig. 4g illustrated the LSPR electromagnetic field was enhanced and the hot spots were mainly located at the catalytic Pt surface, corresponding to the hot electrons transferred from TiO_{2-x} to Pt in the Pt/TiO_{2-x} nanostructure [59,60].

Compared with previously reports (Fig. 4h, Table S2), Pt/TiO_{2-x}/Ti showed perfect performance of 399.2 mmol g⁻¹ h⁻¹ in the infrared region, which was better or close to other catalysts, such as CdS/MoS₂ (PLA 379.35 mmol g⁻¹ h⁻¹, PET 60.8 mmol g⁻¹ h⁻¹) [61], CdS/CdO_x (PLA 64.3 mmol g⁻¹ h⁻¹, PET 12.4 mmol g⁻¹ h⁻¹) [14], M-2/Z_{0.6}C_{0.4}S (PET, 14.2 mmol g⁻¹ h⁻¹) [62], CN_x/Pt (PLA, 0.49 mmol g⁻¹ h⁻¹) [63], CN_x/Ni₂P (PLA, 0.17 mmol g⁻¹ h⁻¹) [63], TiO₂/Pt (PLA, 0.089 mmol g⁻¹ h⁻¹) [14], CN-CNTs-NiMo (PLA, 0.09 mmol g⁻¹ h⁻¹) [64], d-NiPS₃/CdS (PLA 135.11 mmol g⁻¹ h⁻¹, PET 121.04 mmol g⁻¹ h⁻¹) [65] and Pt-CdO_x/CdS/SiC (PE 0.025 mmol g⁻¹ h⁻¹) [66]. It was worth noting that other catalysts were almost tested in visible light or even the full spectrum, Pt/TiO_{2-x}/Ti showed excellent hydrogen production performance in the infrared region.

3.4. Photothermic hydrogen evolution performance under the outdoor sunlight

In order to further determine its practical application value, large-scaled Pt/TiO_{2-x}/Ti with size of 5 × 5 cm² was prepared by laser process, taking advantage of the scalability of laser synthesis (Fig. 5a). In order to demonstrate the homogeneity of large-scaled Pt/TiO_{2-x}/Ti, the catalyst was divided into nine regions, then the morphologies and photothermal properties of different regions were tested. SEM images of nine regions in Fig. 5b indicated that the microstructure of Pt/TiO_{2-x}/Ti was uniform in large area. Infrared thermal images showed that every region of Pt/TiO_{2-x}/Ti could reach ~ 35.2 °C and ~ 256.5 °C under ambient sunlight irradiation without and with Fresnel lens, respectively (Fig. 5c). In addition, the photothermal temperatures of 10 M NaOH aqueous solution with plastic were 34.2 °C and 71.6 °C under ambient sunlight irradiation without and with Fresnel lens, respectively (Fig. S16).

In order to illustrate the practicability of this system, the photothermal catalytic H₂ production by reforming plastic was carried out under ambient sunlight irradiation in consecutive week. The schematic diagram of the constructed photothermal reaction device was shown in Fig. 5d and the linear Fresnel lens with an area of 25 × 25 cm² was used for the concentrator of sunlight. It could be observed that a large number of hydrogen bubbles were produced on the catalyst when the sunlight was focused (Fig. 5e, S17 and Video S3) and could produce 8.1 mL gases

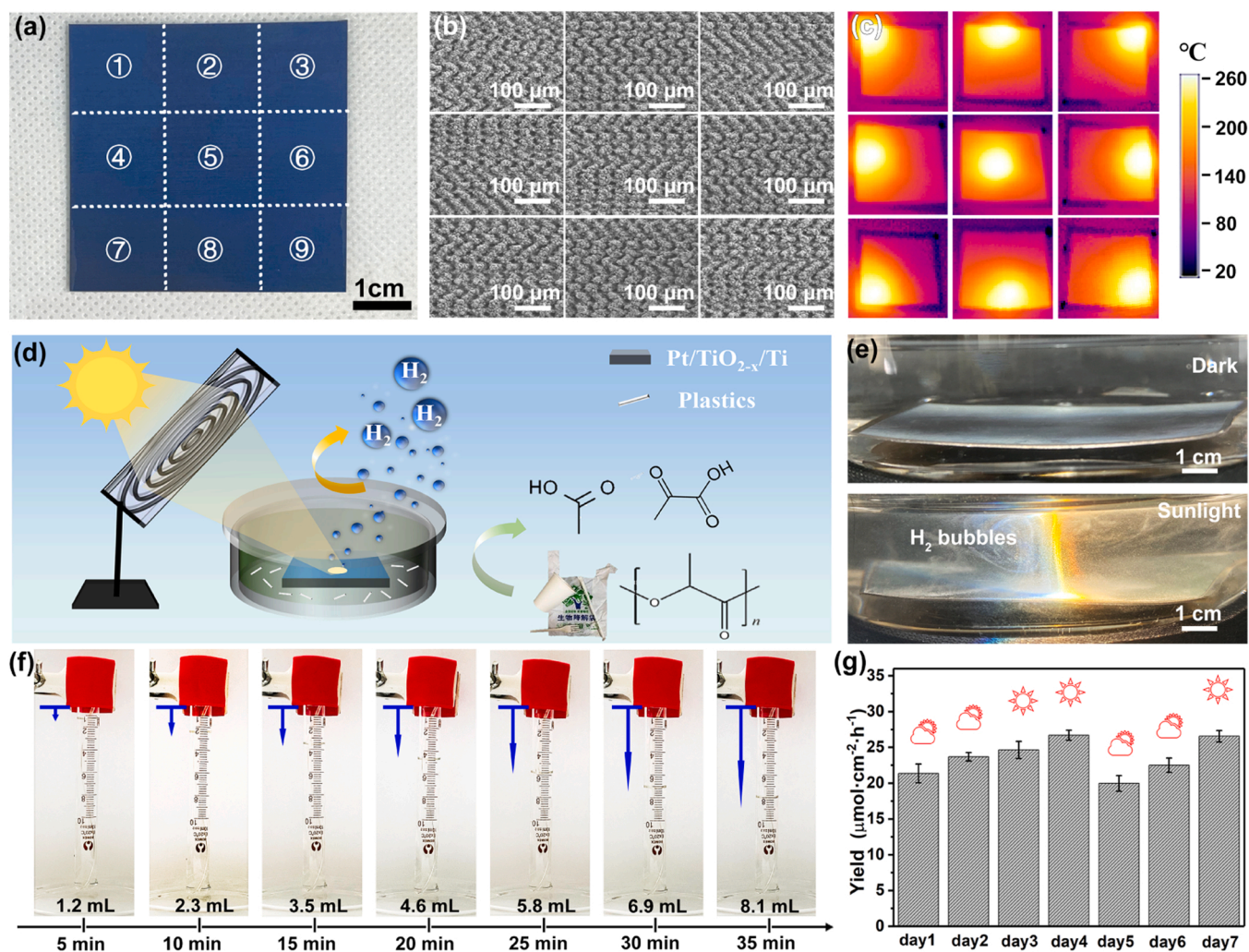


Fig. 5. (a) Optical picture of Pt/TiO_{2-x}/Ti with the size of 5 × 5 cm² divided into nine regions and (b) corresponding SEM images of difference position. (c) IR thermal images of Pt/TiO_{2-x}/Ti under outdoor sunlight irradiation with Fresnel lens. (d) Schematic diagram of constructed photothermal device under the outdoor sunlight. (e) The enlarged optical diagram of Pt/TiO_{2-x}/Ti producing hydrogen. The illustration of this system in action could be found in Supplementary Video. (f) The typical configuration of gas collection for determining volumes of H₂ evolved under outdoor sunlight irradiation with Fresnel lens. (g) H₂ evolution rates of Pt/TiO_{2-x}/Ti under ambient sunlight irradiation in consecutive week (13:00–14:00).



Video S3. Video S3 illustrated a large number of hydrogen bubbles were produced on the Pt/TiO_{2-x}/Ti sheet when the outdoor sunlight was focused..

within 35 min (Fig. 5f). The stability and activity of photothermal H₂ evolution were measured from 13:00–14:00 every day for seven consecutive days. As shown in Fig. 5g, the H₂ evolution rates were about 25.5 μmol cm⁻² h⁻¹ and 19.2 μmol cm⁻² h⁻¹ on sunny days and cloudy

days, respectively.

4. Conclusions

In summary, SAL-Pt clusters were successfully prepared on TiO_{2-x}/Ti support via confinement-anchoring effect of oxygen vacancies. The obtained Pt/TiO_{2-x}/Ti had excellent performance of photothermal hydrogen evolution of 273.12 μmol cm⁻² h⁻¹ from reforming plastic under light irradiation with λ > 760 nm in liquid, which was approximately 17.2 times higher than that of the sample in ultraviolet region (15.87 μmol cm⁻² h⁻¹). During the IR-driven photothermal catalytic process, oxygen vacancies could serve as anchoring sites to atomically dispersed Pt and enhance the light absorption in the infrared regions, then plasmonic hot electrons and high temperature were produced. SAL-Pt clusters served as the catalytic active sites for hydrogen evolution reaction. AFM-KPFM combined with FDTD simulations demonstrated that IR-driven plasmonic hot electron transferred from TiO_{2-x}/Ti to Pt. Furthermore, the system works excellent outdoors with perfect activity and stability, proving the potential of practical applicability of our system. This work provides a novelty avenue to construct oxygen vacancies on metal foil and rationally design fully exposed single-atom-layer clusters. The process presented here could expand the use of

plastic wastes and inspire new upcycling strategies for different plastic wastes.

CRedit authorship contribution statement

Di Jiang preformed the experiments, analyzed the data and wrote the paper. Haifeng Yuan and Zhen Liu preformed the experiments, analyzed the data and discussed the manuscript. Yuke Chen, Yangyang Li, Xiaoli Zhang, Guobin Xue, and Hong Liu discussed the manuscript and supervised the research. Xiaoyan Liu, Lili Zhao and Weijia Zhou designed, conceived and initiated the research.

Declaration of Competing Interest

The authors declare that they have no known competing financial interests or personal relationships that could have appeared to influence the work reported in this paper.

Data Availability

No data was used for the research described in the article.

Acknowledgements

This work was supported by National Natural Science Foundation of China (52022037, 51972147), Taishan Scholar Project of Shandong Province (tsqn201812083), Natural Science Foundation of Shandong Province (ZR2021JQ15, ZR2022YQ42, ZR2020QE057), and Innovative Team Project of Jinan (2021GXRC019).

Appendix A. Supporting information

Supplementary data associated with this article can be found in the online version at doi:10.1016/j.apcatb.2023.123081.

References

- [1] A. Kumar, P. Daw, D. Milstein, Homogeneous catalysis for sustainable energy: hydrogen and methanol economies, fuels from biomass, and related topics, *Chem. Rev.* 122 (2022) 385–441.
- [2] A. Sartbaeva, V.L. Kuznetsov, S.A. Wells, P.P. Edwards, Hydrogen nexus in a sustainable energy future, *Energy Environ. Sci.* 1 (2008) 79–85.
- [3] M. Hermesmann, T.E. Müller, Green, turquoise, blue, or grey? Environmentally friendly hydrogen production in transforming energy systems, *Prog. Energy Combust. Sci.* 90 (2022), 100996.
- [4] J. Qi, W. Zhang, R. Cao, Solar-to-hydrogen energy conversion based on water splitting, *Adv. Energy Mater.* 8 (2018), 1701620.
- [5] Y. Chen, J. Yu, J. Jia, F. Liu, Y. Zhang, G. Xiong, R. Zhang, R. Yang, D. Sun, H. Liu, W. Zhou, Metallic Ni₃Mo₃N porous microtubes with abundant catalytic sites as efficient electrocatalyst for large current density and superstability of hydrogen evolution reaction and water splitting, *Appl. Catal. B Environ.* 272 (2020), 118956.
- [6] M. MacLeod, H. Arp Hans Peter, B. Tekman Mine, A. Jahnke, The global threat from plastic pollution, *Science* 373 (2021) 61–65.
- [7] B. Borrelle Stephanie, J. Ringma, L. Law Kara, C. Monahan Cole, L. Lebreton, A. McGivern, E. Murphy, J. Jambeck, H. Leonard George, A. Hilleary Michelle, M. Eriksen, P. Possingham Hugh, H. De Frond, R. Gerber Leah, B. Polidoro, A. Tahir, M. Bernard, N. Mallos, M. Barnes, M. Rochman Chelsea, Predicted growth in plastic waste exceeds efforts to mitigate plastic pollution, *Science* 369 (2020) 1515–1518.
- [8] C. Horejs, Solutions to plastic pollution, *Nat. Rev. Mater.* 5 (2020), 641–641.
- [9] R. Altman, The myth of historical bio-based plastics, *Science* 373 (2021) 47–49.
- [10] S. Lambert, M. Wagner, Environmental performance of bio-based and biodegradable plastics: the road ahead, *Chem. Soc. Rev.* 46 (2017) 6855–6871.
- [11] T. Iwata, Biodegradable and bio-based polymers: future prospects of eco-friendly plastics, *Angew. Chem., Int. Ed.* 54 (2015) 3210–3215.
- [12] X. Jiao, K. Zheng, Z. Hu, S. Zhu, Y. Sun, Y. Xie, Conversion of waste plastics into value-added carbonaceous fuels under mild conditions, *Adv. Mater.* 33 (2021), 2005192.
- [13] U. Nwosu, A. Wang, B. Palma, H. Zhao, M.A. Khan, M. Kibria, J. Hu, Selective biomass photoreforming for valuable chemicals and fuels: a critical review, *Renew. Sust. Energy Rev.* 148 (2021), 111266.
- [14] T. Uekert, M.F. Kuehn, D.W. Wakerley, E. Reisner, Plastic waste as a feedstock for solar-driven H₂ generation, *Energy Environ. Sci.* 11 (2018) 2853–2857.
- [15] S. Bai, J. Jiang, Q. Zhang, Y. Xiong, Steering charge kinetics in photocatalysis: intersection of materials syntheses, characterization techniques and theoretical simulations, *Chem. Soc. Rev.* 44 (2015) 2893–2939.
- [16] W. Jiang, S. Bai, L. Wang, X. Wang, L. Yang, Y. Li, D. Liu, X. Wang, Z. Li, J. Jiang, Y. Xiong, Integration of multiple plasmonic and Co-catalyst nanostructures on TiO₂ nanosheets for visible-near-infrared photocatalytic hydrogen evolution, *Small* 12 (2016) 1640–1648.
- [17] A. Meng, L. Zhang, B. Cheng, J. Yu, Dual cocatalysts in TiO₂ photocatalysis, *Adv. Mater.* 31 (2019), 1807660.
- [18] Q. Guo, C. Zhou, Z. Ma, X. Yang, Fundamentals of TiO₂ photocatalysis: concepts, mechanisms, and challenges, *Adv. Mater.* 31 (2019), 1901997.
- [19] Q. Sun, N. Wang, J. Yu, J.C. Yu, A hollow porous CdS photocatalyst, *Adv. Mater.* 30 (2018), 1804368.
- [20] P. Zhang, D. Luan, X.W. Lou, Fabrication of CdS frame-in-cage particles for efficient photocatalytic hydrogen generation under visible-light irradiation, *Adv. Mater.* 32 (2020), 2004561.
- [21] H. Liu, J. Yu, Y. Chen, Z. Zhou, G. Xiong, L. Zeng, H. Li, Z. Liu, L. Zhao, J. Wang, B. Chu, H. Liu, W. Zhou, One-step sublimation and epitaxial growth of CdS-Cd heterogeneous nanoparticles on S-doped MoO₃ nanosheets for efficient visible light-driven photocatalytic H₂ generation, *ACS Appl. Mater. Interfaces* 12 (2020) 2362–2369.
- [22] R. Wang, S. Chen, Y.H. Ng, Q. Gao, S. Yang, S. Zhang, F. Peng, Y. Fang, S. Zhang, ZnO/CdS/PbS nanotube arrays with multi-heterojunctions for efficient visible-light-driven photoelectrochemical hydrogen evolution, *Chem. Eng. J.* 362 (2019) 658–666.
- [23] C.-Y. Lee, A.C. Taylor, S. Beirne, G.G. Wallace, 3D-printed conical arrays of TiO₂ electrodes for enhanced photoelectrochemical water splitting, *Adv. Energy Mater.* 7 (2017), 1701060.
- [24] J. Li, M. Zhang, Z. Guan, Q. Li, C. He, J. Yang, Synergistic effect of surface and bulk single-electron-trapped oxygen vacancy of TiO₂ in the photocatalytic reduction of CO₂, *Appl. Catal. B: Environ.* 206 (2017) 300–307.
- [25] T.R. Gordon, M. Cargnello, T. Paik, F. Mangolini, R.T. Weber, P. Fornasiero, C. B. Murray, Nonaqueous synthesis of TiO₂ nanocrystals using TiF₄ to engineer morphology, oxygen vacancy concentration, and photocatalytic activity, *J. Am. Chem. Soc.* 134 (2012) 6751–6761.
- [26] X. Chen, L. Liu, Y. Yu Peter, S. Mao Samuel, Increasing solar absorption for photocatalysis with black hydrogenated titanium dioxide nanocrystals, *Science* 331 (2011) 746–750.
- [27] G. Ou, Y. Xu, B. Wen, R. Lin, B. Ge, Y. Tang, Y. Liang, C. Yang, K. Huang, D. Zu, R. Yu, W. Chen, J. Li, H. Wu, L.-M. Liu, Y. Li, Tuning defects in oxides at room temperature by lithium reduction, *Nat. Commun.* 9 (2018) 1302.
- [28] M. Wajid Shah, Y. Zhu, X. Fan, J. Zhao, Y. Li, S. Asim, C. Wang, Facile synthesis of defective TiO_{2-x} nanocrystals with high surface area and tailoring bandgap for visible-light photocatalysis, *Sci. Rep.* 5 (2015) 15804.
- [29] Z. Zhang, M.N. Hedhili, H. Zhu, P. Wang, Electrochemical reduction induced self-doping of Ti³⁺ for efficient water splitting performance on TiO₂ based photoelectrodes, *Phys. Chem. Chem. Phys.* 15 (2013) 15637–15644.
- [30] M. Liang, X. Li, L. Jiang, P. Ran, H. Wang, X. Chen, C. Xu, M. Tian, S. Wang, J. Zhang, T. Cui, L. Qu, Femtosecond laser mediated fabrication of micro/nanostructured TiO_{2-x} photoelectrodes: hierarchical nanotubes array with oxygen vacancies and their photocatalysis properties, *Appl. Catal. B: Environ.* 277 (2020), 119231.
- [31] V.A. Zuniga-Ibarra, S. Shaji, B. Krishnan, J. Johny, S. Sharma Kanakkilam, D. A. Avellaneda, J.A.A. Martinez, T.K.D. Roy, N.A. Ramos-Delgado, Synthesis and characterization of black TiO₂ nanoparticles by pulsed laser irradiation in liquid, *Appl. Surf. Sci.* 483 (2019) 156–164.
- [32] M. Zimbone, M.A. Buccheri, G. Cacciato, R. Sanz, G. Rappazzo, S. Boninelli, R. Reitano, L. Romano, V. Privitera, M.G. Grimaldi, Photocatalytic and antibacterial activity of TiO₂ nanoparticles obtained by laser ablation in water, *Appl. Catal. B: Environ.* 165 (2015) 487–494.
- [33] L. Zhao, Z. Liu, D. Chen, F. Liu, Z. Yang, X. Li, H. Yu, H. Liu, W. Zhou, Laser synthesis and microfabrication of micro/nanostructured materials toward energy conversion and storage, *Nanomicro Lett.* 13 (2021) 49.
- [34] Y.J. Kwon, H.W. Kim, W.C. Ko, H. Choi, Y.-H. Ko, Y.K. Jeong, Laser-engineered oxygen vacancies for improving the NO₂ sensing performance of SnO₂ nanowires, *J. Mater. Chem. A* 7 (2019) 27205–27211.
- [35] Y. Chen, Y. Wang, J. Yu, G. Xiong, H. Niu, Y. Li, D. Sun, X. Zhang, H. Liu, W. Zhou, Underfocus laser induced Ni nanoparticles embedded metallic MoN microrods as patterned electrode for efficient overall water splitting, *Adv. Sci.* 9 (2022), 2105869.
- [36] H. Palneedi, J.H. Park, D. Maurya, M. Peddigari, G.-T. Hwang, V. Annappureddy, J.-W. Kim, J.-J. Choi, B.-D. Hahn, S. Priya, K.J. Lee, J. Ryu, Laser irradiation of metal oxide films and nanostructures: applications and advances, *Adv. Mater.* 30 (2018), 1705148.
- [37] Z. Li, Y. Zhang, Y. Feng, C.-Q. Cheng, K.-W. Qiu, C.-K. Dong, H. Liu, X.-W. Du, Co₃O₄ nanoparticles with ultrasmall size and abundant oxygen vacancies for boosting oxygen involved reactions, *Adv. Funct. Mater.* 29 (2019), 1903444.
- [38] Z. Tian, Y. Da, M. Wang, X. Dou, X. Cui, J. Chen, R. Jiang, S. Xi, B. Cui, Y. Luo, H. Yang, Y. Long, Y. Xiao, W. Chen, Selective photoelectrochemical oxidation of glucose to glucaric acid by single atom Pt decorated defective TiO₂, *Nat. Commun.* 14 (2023) 142.
- [39] X. Shi, Y. Huang, Y. Bo, D. Duan, Z. Wang, J. Cao, G. Zhu, W. Ho, L. Wang, T. Huang, Y. Xiong, Highly selective photocatalytic CO₂ methanation with water vapor on single-atom platinum-decorated defective carbon nitride, *Angew. Chem. Int. Ed.* 61 (2022), e202203063.

- [40] J. Chen, Y. Kang, W. Zhang, Z. Zhang, Y. Chen, Y. Yang, L. Duan, Y. Li, W. Li, Lattice-confined single-atom Fe1Sx on mesoporous TiO₂ for boosting ambient electrocatalytic N₂ reduction reaction, *Angew. Chem. Int. Ed.* 61 (2022), e202203022.
- [41] J. Wan, W. Chen, C. Jia, L. Zheng, J. Dong, X. Zheng, Y. Wang, W. Yan, C. Chen, Q. Peng, D. Wang, Y. Li, Defect effects on TiO₂ nanosheets: stabilizing single atomic site Au and promoting catalytic properties, *Adv. Mater.* 30 (2018), 1705369.
- [42] L. Duan, C.-T. Hung, J. Wang, C. Wang, B. Ma, W. Zhang, Y. Ma, Z. Zhao, C. Yang, T. Zhao, L. Peng, D. Liu, D. Zhao, W. Li, Synthesis of fully exposed single-atom-layer metal clusters on 2D ordered mesoporous TiO₂ nanosheets, *Angew. Chem. Int. Ed.* (2022), e202211307.
- [43] X. Chen, M. Peng, X. Cai, Y. Chen, Z. Jia, Y. Deng, B. Mei, Z. Jiang, D. Xiao, X. Wen, N. Wang, H. Liu, D. Ma, Regulating coordination number in atomically dispersed Pt species on defect-rich graphene for n-butane dehydrogenation reaction, *Nat. Commun.* 12 (2021) 2664.
- [44] X. Cheng, Y. Lu, L. Zheng, M. Pucupski, H. Li, G. Chen, S. Sun, G. Wu, Engineering local coordination environment of atomically dispersed platinum catalyst via lattice distortion of support for efficient hydrogen evolution reaction, *Mater. Today Energy* 20 (2021), 100653.
- [45] Q. Yang, H. Liu, P. Yuan, Y. Jia, L. Zhuang, H. Zhang, X. Yan, G. Liu, Y. Zhao, J. Liu, S. Wei, L. Song, Q. Wu, B. Ge, L. Zhang, K. Wang, X. Wang, C.-R. Chang, X. Yao, Single carbon vacancy traps atomic platinum for hydrogen evolution catalysis, *J. Am. Chem. Soc.* 144 (2022) 2171–2178.
- [46] X. Liu, C. Xing, F. Yang, Z. Liu, Y. Wang, T. Dong, L. Zhao, H. Liu, W. Zhou, Strong interaction over Ru/defects-rich aluminium oxide boosts photothermal CO₂ methanation via microchannel flow-type system, *Adv. Energy Mater.* 12 (2022), 2201009.
- [47] Z. Luo, G. Zhao, H. Pan, W. Sun, Strong metal-support interaction in heterogeneous catalysts, *Adv. Energy Mater.* N/a (2022), 2201395.
- [48] Y. Chen, S. Ji, W. Sun, Y. Lei, Q. Wang, A. Li, W. Chen, G. Zhou, Z. Zhang, Y. Wang, L. Zheng, Q. Zhang, L. Gu, X. Han, D. Wang, Y. Li, Engineering the atomic interface with single platinum atoms for enhanced photocatalytic hydrogen production, *Angew. Chem. Int. Ed.* 59 (2020) 1295–1301.
- [49] L. Duan, C.-T. Hung, J. Wang, C. Wang, B. Ma, W. Zhang, Y. Ma, Z. Zhao, C. Yang, T. Zhao, L. Peng, D. Liu, D. Zhao, W. Li, Synthesis of fully exposed single-atom-layer metal clusters on 2D ordered mesoporous TiO₂ nanosheets, *Angew. Chem. Int. Ed.* 61 (2022), e202211307.
- [50] M. Cai, W. Liu, X. Luo, C. Chen, R. Pan, H. Zhang, M. Zhong, Correction to “three-dimensional and in situ-activated spinel oxide nanoporous clusters derived from stainless steel for efficient and durable water oxidation”, *ACS Appl. Mater. Interfaces* 12 (2020), 19243–19243.
- [51] Z. Hu, K. Li, X. Wu, N. Wang, X. Li, Q. Li, L. Li, K. Lv, Dramatic promotion of visible-light photoreactivity of TiO₂ hollow microspheres towards NO oxidation by introduction of oxygen vacancy, *Appl. Catal. B: Environ.* 256 (2019), 117860.
- [52] Y. Yang, L.-C. Yin, Y. Gong, P. Niu, J.-Q. Wang, L. Gu, X. Chen, G. Liu, L. Wang, H.-M. Cheng, An unusual strong visible-light absorption band in red anatase TiO₂ photocatalyst induced by atomic hydrogen-occupied oxygen vacancies, *Adv. Mater.* 30 (2018), 1704479.
- [53] T. Dong, X. Liu, Z. Tang, H. Yuan, D. Jiang, Y. Wang, Z. Liu, X. Zhang, S. Huang, H. Liu, L. Zhao, W. Zhou, Ru decorated TiOx nanoparticles via laser bombardment for photothermal co-catalytic CO₂ hydrogenation to methane with high selectivity, *Appl. Catal. B: Environ.* 326 (2023), 122176.
- [54] N. Zhou, R. Wang, X. Zhou, H. Song, X. Xiong, Y. Ding, J. Lü, L. Gan, T. Zhai, P-GaSe/N-MoS₂ vertical heterostructures synthesized by van der Waals epitaxy for photoresponse modulation, *Small* 14 (2018), 1702731.
- [55] G. Wang, L. Li, W. Fan, R. Wang, S. Zhou, J.T. Lü, L. Gan, T. Zhai, Interlayer coupling induced infrared response in WS₂/MoS₂ heterostructures enhanced by surface plasmon resonance, *Adv. Funct. Mater.* 28 (2018), 1800339.
- [56] B. Xia, B. He, J. Zhang, L. Li, Y. Zhang, J. Yu, J. Ran, S.Z. Qiao, TiO₂/FePS₃ S-scheme heterojunction for greatly raised photocatalytic hydrogen evolution, *Adv. Energy Mater.* 12 (2022), 2201449.
- [57] T. Zhou, P. Zhang, D. Zhu, S. Cheng, H. Dong, Y. Wang, G. Che, Y. Niu, M. Yan, C. Li, Synergistic effect triggered by skeleton delocalization and edge induction of carbon nitride expedites photocatalytic hydrogen evolution, *Chem. Eng. J.* 442 (2022), 136190.
- [58] C. Li, H. Wu, D. Zhu, T. Zhou, M. Yan, G. Chen, J. Sun, G. Dai, F. Ge, H. Dong, High-efficient charge separation driven directionally by pyridine rings grafted on carbon nitride edge for boosting photocatalytic hydrogen evolution, *Appl. Catal. B* 297 (2021), 120433.
- [59] Y. Tang, W. Zhou, Q. Shang, Y. Guo, H. Hu, Z. Li, Y. Zhang, L. Liu, H. Wang, X. Tan, T. Yu, J. Ye, Discerning the mechanism of expedited interfacial electron transformation boosting photocatalytic hydrogen evolution by metallic 1T-WS₂-induced photothermal effect, *Appl. Catal. B: Environ.* 310 (2022), 121295.
- [60] W. Gao, Q. Liu, X. Zhao, C. Cui, S. Zhang, W. Zhou, X. Wang, S. Wang, H. Liu, Y. Sang, Electromagnetic induction effect induced high-efficiency hot charge generation and transfer in Pd-tipped Au nanorods to boost plasmon-enhanced formic acid dehydrogenation, *Nano Energy* 80 (2021), 105543.
- [61] L. Zhao, T. Dong, J. Du, H. Liu, H. Yuan, Y. Wang, J. Jia, H. Liu, W. Zhou, Synthesis of CdS/MoS₂ nanooctahedrons heterostructure with a tight interface for enhanced photocatalytic H₂ evolution and biomass upgrading, *Sol. RRL* 5 (2021), 2000415.
- [62] B. Cao, S. Wan, Y. Wang, H. Guo, M. Ou, Q. Zhong, Highly-efficient visible-light-driven photocatalytic H₂ evolution integrated with microplastic degradation over MXene/Zn₃Cd_{1-x}S photocatalyst, *J. Colloid Interface Sci.* 605 (2022) 311–319.
- [63] T. Uekert, H. Kasap, E. Reisner, Photoreforming of nonrecyclable plastic waste over a carbon nitride/nickel phosphide catalyst, *J. Am. Chem. Soc.* 141 (2019) 15201–15210.
- [64] X. Gong, F. Tong, F. Ma, Y. Zhang, P. Zhou, Z. Wang, Y. Liu, P. Wang, H. Cheng, Y. Dai, Z. Zheng, B. Huang, Photoreforming of plastic waste poly (ethylene terephthalate) via in-situ derived CN-CNTs-NiMo hybrids, *Appl. Catal. B: Environ.* 307 (2022), 121143.
- [65] S. Zhang, H. Li, L. Wang, J. Liu, G. Liang, K. Davey, J. Ran, S.-Z. Qiao, Boosted photoreforming of plastic waste via defect-rich NiPS₃ nanosheets, *J. Am. Chem. Soc.* 145 (2023) 6410–6419.
- [66] H. Nagakawa, M. Nagata, Photoreforming of organic waste into hydrogen using a thermally radiative CdO_x/CdS/SiC photocatalyst, *ACS Appl. Mater. Interfaces* 13 (2021) 47511–47519.